

## Article

# Calcium Ions Modulate the Mechanics of Tomato Bushy Stunt Virus

Aida Llauro,<sup>1</sup> Emilia Coppari,<sup>2</sup> Francesca Imperatori,<sup>3</sup> Anna R. Bizzarri,<sup>2</sup> José R. Castón,<sup>4</sup> Luca Santi,<sup>3</sup> Salvatore Cannistraro,<sup>2</sup> and Pedro J. de Pablo<sup>1,\*</sup>

<sup>1</sup>Department of Condensed Matter Physics and Condensed Matter Physics Center (IFIMAC), Universidad Autónoma de Madrid, Madrid, Spain; <sup>2</sup>Biophysics and Nanoscience Centre, CNISM-DEB, Università della Tuscia, Viterbo, Italy; <sup>3</sup>Department of Agriculture, Forests, Nature and Energy (DAFNE), Università della Tuscia, Viterbo, Italy; and <sup>4</sup>Department of Macromolecular Structure, Centro Nacional de Biotecnología/CSIC, Madrid Spain

**ABSTRACT** Viral particles are endowed with physicochemical properties whose modulation confers certain metastability to their structures to fulfill each task of the viral cycle. Here, we investigate the effects of swelling and ion depletion on the mechanical stability of individual tomato bushy stunt virus nanoparticles (TBSV-NPs). Our experiments show that calcium ions modulate the mechanics of the capsid: the sequestration of calcium ions from the intracapsid binding sites reduces rigidity and resilience in ~24% and 40%, respectively, of TBSV-NPs. Interestingly, mechanical deformations performed on native TBSV-NPs induce an analogous result. In addition, TBSV-NPs do not show capsomeric vacancies after surpassing the elastic limit. We hypothesize that even though there are breakages among neighboring capsomers, RNA-capsid protein interaction prevents the release of capsid subunits. This work shows the mechanical role of calcium ions in viral shell stability and identifies TBSV-NPs as malleable platforms based on protein cages for cargo transportation at the nanoscale.

## INTRODUCTION

Viral capsids are self-assembled macromolecular shells that naturally protect, shuttle, and release the enclosed genetic material under the proper physicochemical conditions (1). The stability of viral shells has been tuned by evolution to respond to a variety of environmental conditions encountered along their biological cycle. This enormous adaptability to the environment, together with the possibility of genetically engineering their coat protein (CP) coding sequence, have made viruses attractive systems for constructing virus-derived nanoparticles (VNPs) for applications in bionanotechnology (2). Among them, plant virus capsids display a variety of properties particularly appropriate for application in nanotechnology, such as their controllable genetic manipulability, their inability to infect and replicate in vertebrate hosts, and their ease of production (3). Tomato bushy stunt virus nanoparticles (TBSV-NPs) are robust, stable, highly modifiable, and easy to manufacture using *Nicotiana benthamiana* as the production host (4). In addition, the intrinsic tendency of these viruses to form ordered aggregates has been used already to build homogeneous monolayers (5).

TBSV is a small nonenveloped virus with an outer diameter of ~33 nm and an icosahedral symmetry with a triangulation number of  $T = 3$  (Fig. 1 A, left). The viral capsid is formed by the assembly of 180 subunits of a single CP

and its genome consists of a monopartite single-stranded RNA (ssRNA) (6). An attractive feature of TBSV-NPs is that their inner cavity can be accessed using a swelling process that mediates reversible opening of pores on the VNP surface (Fig. 1 A, right) (7). This process, which likely occurs during the first stages of the infection cycle, increases the virus dimension through a  $\text{Ca}^{2+}$ -dependent transition, and it is required for the release of the RNA during uncoating (8). The subunits of TBSV are arranged in three packing environments: A-, B-, and C-subunits (Fig. 1 B). A-subunits (blue) pack around the fivefold symmetry axes, whereas B- and C-subunits (white and green, respectively) pack alternatively around the threefold symmetry axes. Each capsomeric subunit is divided into three regions: the P-domain, which protrudes outward, giving the virus a granular appearance; the S-domain, which forms the shell; and the R-domain, an inner tail protein that is inserted into the viral RNA (7).

Investigating virus physicochemical properties under different conditions is a cornerstone in the application of these nanostructures for human benefit. In particular, the study of virus mechanics by atomic force microscopy (AFM) (9) has emerged as a powerful technique to unravel the structural role of nucleic acids (10,11) or capsid mutations (12,13). Moreover, AFM has contributed to understanding the influence of environmental conditions on the stability of viruses, including pH variations (14–16) and humidity (17). The study of the mechanical properties of viral shells pivots on the measurement of the stiffness and the breaking force of the particle, which are both determined by recording indentation curves that result from squeezing the particles

Submitted October 23, 2014, and accepted for publication May 30, 2015.

\*Correspondence: [p.j.depablo@uam.es](mailto:p.j.depablo@uam.es)

Aida Llauro and Emilia Coppari contributed equally to this work.

Editor: Nathan Baker.

© 2015 by the Biophysical Society  
0006-3495/15/07/0001/8 \$2.00

<http://dx.doi.org/10.1016/j.bpj.2015.05.039>

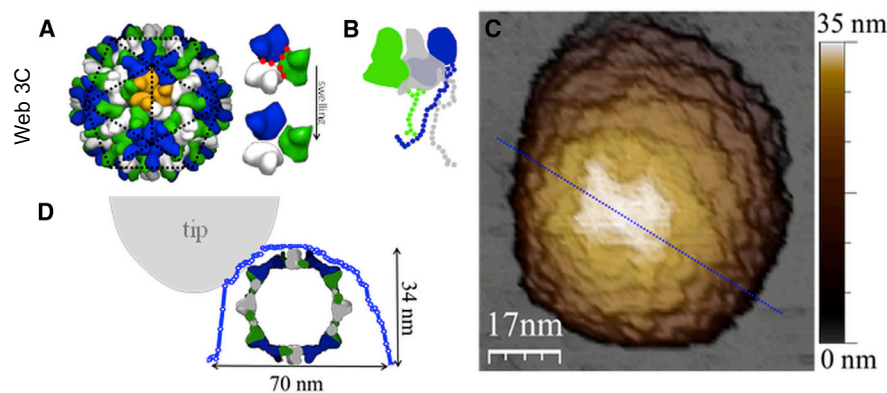


**FIGURE 1** TBSV structure. (A) (Left) Side view derived from x-ray diffraction data (Protein Data Bank 2TBV) (31). One of the protein trimers at the quasi-threefold axes is drawn in orange in the structure. The black dashed lines drawn on the particle help to extrapolate the triangulation number (T) of the virus, which describes the distribution of the capsomers on the surface of an icosahedral virus. For TBSV-NPs,  $T = 3$ . (Right) Sketch of the conformational change associated with the swelling process. The subunits of the trimer before expansion are tightly packed and the  $\text{Ca}^{2+}$ -binding sites include the ions (red dots) (upper). After the expansion, the  $\text{Ca}^{2+}$  ions are removed and the electrostatic repulsion between subunits opens pores at the quasithreefold axes (lower). (B) Sketch of a

trimer. Each trimer is composed of A-, B-, and C-type protein subunits: the A-type are packed around the fivefold axes (blue), and the B- and C-types alternate around the threefold axes (gray and green, respectively). (C) JM-AFM image of compacted wild-type VNPs in liquid conditions. The dotted blue line shows the profile along which the height was determined. The minimal resolved feature on the virus is  $\sim 5$  nm. (D) Profile of the particle in (B) taken along its central part (blue circles). The tip geometrically dilates the lateral dimension of the particle. To see this figure in color, go online.

with an AFM tip. The stiffness (directly linked to the spring constant of the viral particle) (18) is obtained from the linear regime of the deformation and permits determination of the rigidity of the capsid (9). On the other hand, the breaking force, which is defined as the force needed to disrupt the capsids, corresponds to the end of the elastic regime (19) and provides information about the strength of the capsid.

In this article, we present a twofold study in which topographic and mechanical analyses were used to probe the stability of individual TBSV-NPs in different conditions, such as pH and the chelation of calcium ions. Our results reveal that the intracapsid calcium ions are inextricably linked to both virus rigidity and elastic limit. In addition, we show that viral particles keep their capsomers after irreversible deformation, a valuable feature of these systems that makes them usable as malleable nanocarriers for drug delivery.

## MATERIALS AND METHODS

### TBSV wild-type

Infectious complementary DNA (cDNA) clones were assembled using standard recombinant DNA techniques described in detail by Grasso et al. (4).

### Plant infection

Six- to eight-week-old *Nicotiana benthamiana* plants were inoculated with two different TBSV constructs (4). Briefly, cDNA templates of TBSV wild-type constructs were digested with the restriction enzyme XmaI. One  $\mu\text{g}$  of completely linearized cDNA was used for in vitro transcription reaction according to the manufacturer instructions (MEGAscript T7 High Yield Transcription kit, Ambion Applied Biosystems, Foster City, CA). Plants were mechanically inoculated by abrading the adaxial side of two leaves per plant using carborundum powder (VWR International, Radnor, PA) mixed with TBSV infectious RNAs previously checked for integrity by TBE denaturing agarose gel electrophoresis.

### Virus purification

Virus purification was carried out as described by Grasso et al. (4). Briefly, infected tissue was ground in liquid nitrogen and homogenized with 3 mL/g of ice-cold extraction buffer (50 mM sodium acetate, 1% (w/v) ascorbic acid, pH 4.5, supplemented with a cocktail of protease inhibitors (P9599, Sigma, St. Louis, MO)) Homogenate was immediately filtered through Miracloth, and after low-speed centrifugation, the supernatant was adjusted to pH 5.0 with NaOH and ultracentrifuged for 1 h at  $90,000 \times g$  at  $4^\circ\text{C}$ , using a Sorvall WX ULTRA 100 ultracentrifuge (Thermo Scientific, Waltham, MA) with an AH629 rotor. The pellet was gently suspended in ice-cold acetate buffer (50 mM sodium acetate, pH 5.3) and then centrifuged at low speed for further clarification. Quality of the preparations was verified by silver-stained 13.5% sodiumdodecylsulfate polyacrylamide gel electrophoresis (Fig. S1 in the Supporting Material). Viral particle concentration was quantified using Bradford reagent (Bio-Rad, Hercules, CA) and bovine serum albumin as reference standards.

### Sample preparation for AFM measurements

We studied four different forms of TBSV-NPs: compact wild-type TBSV-NPs, swollen wild-type TBSV-NPs, recompact wild-type TBSV-NPs, and  $\text{Ca}^{2+}$ -free wild-type TBSV-NPs (Table S1). All the AFM experiments were conducted in acidic buffer (5 mM  $\text{NiCl}_2$  and 50 mM sodium acetate, pH 5.3), except in the case of swollen TBSV-NPs, where swelling buffer (0.1 M TRIS-HCl, pH 8.5, and 50 mM EDTA) was used.

#### Compact wild-type VNPs

Stock VNP solution (3  $\mu\text{g}/\mu\text{L}$  in 50 mM sodium acetate, pH 5.3) was diluted 1:100 into the acidic buffer (5 mM  $\text{NiCl}_2$  and 50 mM sodium acetate, pH 5.3). A 20  $\mu\text{L}$  drop of this diluted solution was incubated on a freshly cleaved mica surface for 30 min and then gently rinsed with the same buffer. The tip was also pretreated with a drop of 20  $\mu\text{L}$  of the acidic buffer before starting AFM measurements.

#### Swollen wild-type VNPs

Stock compacted wild-type VNP (cVNP) solution was diluted 1:10 in swelling buffer and incubated for 2 h at  $4^\circ\text{C}$ . Then, the solution was diluted 1:10 in swelling buffer in the presence of  $\text{NiCl}_2$  (0.1 M Tris-HCl, pH 8.5, 50 mM EDTA, and 5 mM  $\text{NiCl}_2$ ) before incubating a 20  $\mu\text{L}$  drop of this solution on the mica surface. After 30 min, the sample was washed with swelling buffer, always maintaining an aqueous environment. The tip was pretreated with a 20  $\mu\text{L}$  drop of swelling buffer.

### Recompact wild-type VNPs

The swollen VNPs (stock cVNPs diluted 1:10 in swelling buffer for 2 h at 4°C) were diluted 1:10 into compacting buffer (200 mM CaCl<sub>2</sub> and 50 mM Na-acetate, pH 5.3) and incubated for 2 h at 4°C. Afterward, the solution was diluted 1:2 into acidic buffer and a 20 μL drop of this solution was placed on a cleaved mica surface. After 30 min, the sample was washed with the acidic buffer.

### Ca<sup>2+</sup>-free wild-type VNPs

Stock wild-type cVNP solution was diluted 1:10 in swelling buffer and incubated for 2 h at 4°C. Afterward, the solution was diluted 1:10 into acidic buffer. A 20 μL drop of this diluted solution was deposited on a freshly cleaved mica surface and washed with acidic buffer after 30 min. The swelling buffer promoted the deprotonation of the aspartate residues of the calcium-binding sites (pH 8.5) and the consecutive sequestration of the Ca<sup>2+</sup> ions by the EDTA, which in this case were not added when lowering the pH conditions.

### AFM experiments

All measurements were conducted with an AFM (Nanotec Electrónica, Madrid, Spain) operated in jumping mode (JM) plus for imaging in liquid (20). The relevant feature of this mode is that the lateral displacement of the tip occurs when it is not in contact with the sample, so that shear forces are mostly avoided during scanning. We used rectangular cantilevers (RC800PSA, Olympus, Center Valley, PA) with a nominal spring constant of 0.7 N/m and a tip radius of ~15 nm. These cantilevers were chosen because their spring constant was similar to the spring constant of the virus. The spring constant of the cantilever was calibrated according to the methods of Sader and colleagues (21). The imaging force was typically set at 200 pN.

To carry out the nanoindentation experiments, we followed well-established procedures of virus mechanics (18,22). In brief, they consist of performing a single force-versus-distance curve (FDC) at the very top of a single virus while recording the force as a function of the Z-piezo motion (18). All FDCs were performed at the same Z-piezo displacement (~17 nm) with a loading rate of ~60 nm/s. These FDCs can be converted into force-versus-indentation curves (FICs) by recording a calibration FDC of the cantilever deflection on the substrate next to the virus (9). From fitting the slope of the linear part of the FIC, it is possible to calculate the spring constant (rigidity) of the virus ( $k_v$ ). The steps in the indentation curve that follow the linear region after the elastic limit (19) are interpreted as rupture events (23,24) ranging from big cracks (25) to removal of single capsomers (26). The linear part of the FICs is sometimes preceded by a short-range nonlinear region due to electrostatic, van der Waals, and hydration forces (27,28), which was excluded from the fitting.

During the first five deformations, the VNP was imaged before and after each FIC. From there on, the particle was cyclically loaded and images were taken after sets of five FICs. We stopped the loading experiments when the particle responded with a Hertzian behavior (29). All the images were analyzed using the program WSxM (Nanotec Electrónica) (30); and the profile along the top of the VNP was determined by averaging the height of a five-pixel radius of influence.

### Transmission electron microscopy

For conventional transmission electron microscopy (TEM), 5 μL samples were applied to glow-discharged carbon-coated grids and negatively stained with 2% aqueous uranyl acetate. Samples were applied on carbon-coated grids under the same conditions in which they were adsorbed on mica substrates for AFM measurements. Images were acquired on a JEM-1011 electron microscope (JEOL, Tokyo, Japan) operated at 100 kV, with a 4K X 2.7K ES1000W Erlangshen CCD camera (Gatan, Pleasanton, CA) at a nominal magnification of 24,000×.

## RESULTS

### Topographic characterization

The high-resolution AFM image of a single wild-type cVNP on mica (Fig. 1 C) presents a diameter (height) fully compatible with the nominal size obtained from the x-ray structure (31), where data from millions of different particles are averaged. The granular structure observed in this image might be attributed to the protruding domains (P-domains) present on the outer shell of the TBSV-NP. Therefore, despite the tip-particle lateral dilation (32) (Fig. 1 D), we are able to resolve features of ~5 nm, which correspond to the size of individual capsomers (26,33,34). This resolution was routinely obtained with different tips (Fig. S2).

We studied the stability of the different TBSV-NP forms under distinct environmental conditions using AFM in a liquid milieu and TEM (Fig. 2). AFM images reveal that cVNPs and recompact wild-type VNPs (rVNPs) presented the same average height, which corresponds to the size of intact particles (Fig. 2 C, blue and red dots, respectively), also proving the structural reversibility of the swelling process. In contrast, AFM images of swollen wild-type VNPs (sVNPs) showed collapsed structures with an average height of ~10 nm (Fig. 2 C, black dot), suggesting that the swelling process made these particles feebler. TEM images show that the structural integrity of sVNP particles was less preserved, as negative staining agent penetrated inside the particles, some of which were partially broken (Fig. 2 B, arrows). TEM images of wild-type cVNPs and rVNPs also showed that these particles maintained their structural stability, again providing evidence of the reversibility of the swelling process.

We studied the effect of removing divalent ions from the viral shell by decreasing the pH of VNPs in the absence of calcium ions. This gives rise to an intermediate form between the compact and the swollen state. In this case, the AFM images showed that most of the Ca<sup>2+</sup>-free wild-type VNPs (ifVNPs) maintained their virus-like structure, with an average height of ~30 nm (Fig. 2 C, green dot). However, the existence of debris on the mica substrate—probably material derived from collapsed particles—suggested that some of the particles were less stable. Likewise, TEM images showed that these particles maintained their stability and showed the presence of debris.

### Mechanics

Nanoindentation experiments relied on squeezing individual VNPs with an AFM tip while registering the cantilever deflection versus the piezo displacement (9). The resulting FICs provide information on the mechanical properties of the particle, such as stiffness and the elastic limit. Fig. 3 shows the mechanical and topographical evolution of a wild-type cVNP and an ifVNP. The consecutive FICs

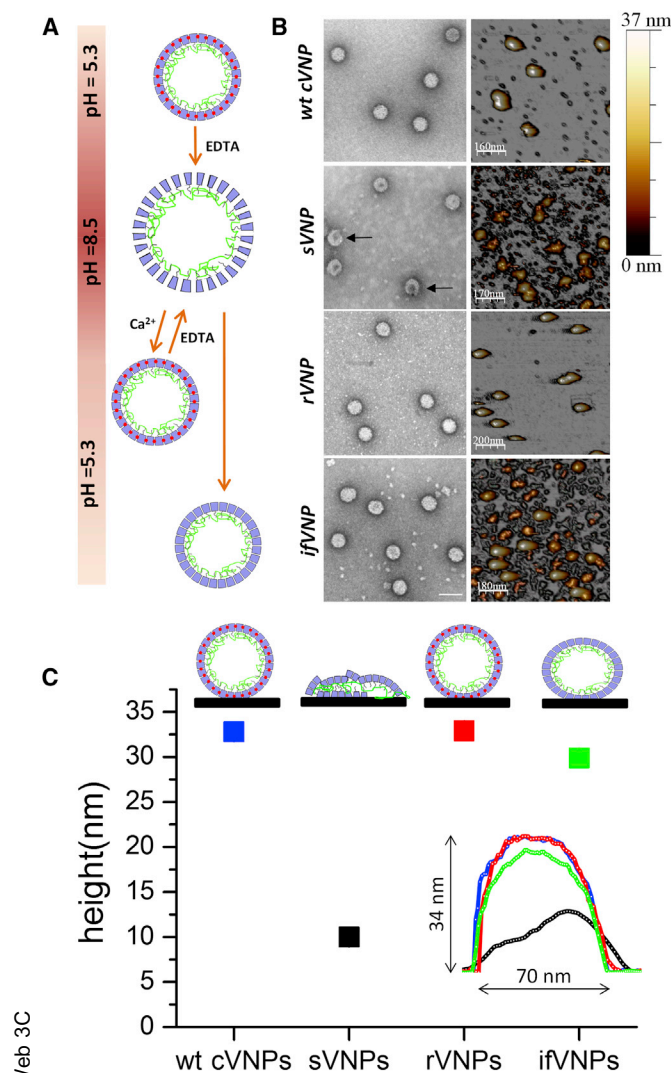


**FIGURE 2** Schematic representation of the swelling process and AFM and TEM images of the particles along this process. (A) Representation of the pH-induced expanding-compacting process. Under acidic conditions (pH 5.3), the Ca<sup>2+</sup> ions are located at specific binding sites (red dots), contributing with an attractive component to the protein-protein interaction. The swelling of the particle was achieved by increasing the pH in the presence of EDTA (7,8,44). This procedure promotes the expansion of the capsid as a consequence of the deprotonation of the aspartate residues at the calcium-binding sites and the subsequent sequestration of these ions. The swollen forms were either 1) recompacted by lowering the pH in the presence of calcium (rVNPs) or 2) compacted by lowering the pH in the absence of calcium ions (ifVNPs). (B) (Left) TEM images of the different forms of the particles. (Scale bar, 50 nm). (Right) AFM images of the different forms of the TBSV-NPs. Images of wild-type cVNPs, rVNPs, and ifVNPs were taken at pH 5.3. Images of sVNPs were taken at pH 8.5. (C) Graph of the heights of the different forms by AFM. (Inset) Profiles of the different forms of TBSV-NPs taken along the central part of each particle. To see this figure in color, go online.

performed on the wild-type cVNP (Fig. 3 A) show that the mechanical response evolves gradually from a linear deformation (FIC 1) to a Hertzian behavior (FIC 10). FIC 1 responds linearly until it reaches a force of ~4.8 nN, where

a sharp drop of the force is registered (elastic limit). The elastic limit is ascribed to the breakage of the particle, which implies the shell cracking (35) or the loss of various capsomers (26,36). However, in this case, immediate imaging of the particle demonstrates the absence of capsomeric vacancies and a height decrease of <2 nm (Fig. 3, B and C). Despite the presence of all the capsomers of the capsids, the backward curve (blue line) defines a hysteresis loop characteristic of nonequilibrium processes such as damage (35) or buckling transitions (23). Some protein cages are able to recover completely after a breakage in times shorter than the time required for taking an image (37), but that is not the scenario seen here. FIC 2 shows a decrease in the elastic limit (~2 nN) and rigidity that indicates some damage to the structure. Therefore, FIC 1 induces a rupture between capsomers that is beyond our AFM imaging resolution but that can be detected by probing the mechanical properties. This argument is further supported by the topographies obtained after each FIC. These images reveal that up to FIC 10, structural damages are limited to the progressive reduction in height without showing capsomeric vacancies (Fig. 3, B and C). Likewise, Fig. S3 confirms the absence of capsomeric vacancies and the progressive loss of height in three different wild-type cVNPs subjected to cyclic loading. In addition, we observe that the data for FICs 7–10 present a monotonic nonlinear mechanical response, which indicates that the capsid can no longer be considered as a shell but must be seen as a solid object (38).

The first deformation, FIC 1, performed on ifVNP shows a lower elastic limit (Fig. 3 D) than in wild-type cVNP. On the other hand, the topographical evolution of this particle throughout the consecutive loading also reveals an irreversible decrease in height without showing capsomeric vacancies until the final FICs (Fig. 3, E and F).

An ensemble analysis helps to generalize some features of our experiments. Fig. 4, A and B, shows the initial three FICs performed on 11 wild-type cVNPs and 16 ifVNPs, respectively. The comparison of the elastic limit throughout the loading cycles (Fig. 4 C) shows that wild-type cVNPs present a higher elastic limit than ifVNPs during the first deformation (FIC 1) but similar limits in subsequent FICs (FICs 2 and 3). Fig. 4 D depicts the evolution of the spring constant of the wild-type cVNPs (black line) and the ifVNPs (blue line). Although the stiffness decreases monotonically for both kinds of particles, wild-type cVNPs start with a higher elastic constant. Finally, the evolution of the height (Fig. 4 E) reveals a progressive deformation of wild-type cVNPs and ifVNPs, with a greater average height for wild-type cVNPs at the beginning, in agreement with Fig. 2 C.

## DISCUSSION

Our results can be discussed from a double perspective, including the topographical aspects of the viral particle

Web 3C

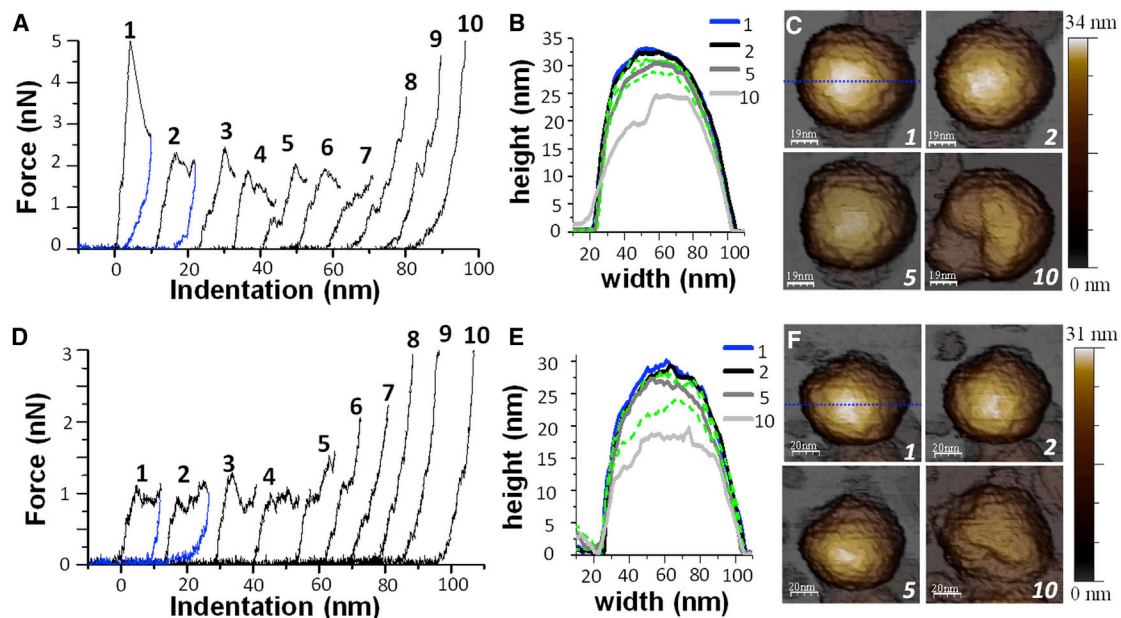


FIGURE 3 Cyclic loading with the single-indentation assay. (A) Cyclic loading performed on a wild-type cVNP. (B and C) Profile and topographic evolution, respectively, of the wild-type cVNP during consecutive loading. Profiles were taken on top of the VNP structures (marked with a dotted blue line in C) and are labeled according to the number of FICs performed on them (i.e., the profile labeled as 1 shows the topography in which FIC-1 was performed). (D–F) The same experiment performed on an ifVNP. All the images were acquired in JM-AFM under acidic buffer conditions (pH 5.3). Indentation curves of (A) and (D) are laterally shifted for clarity. To see this figure in color, go online.

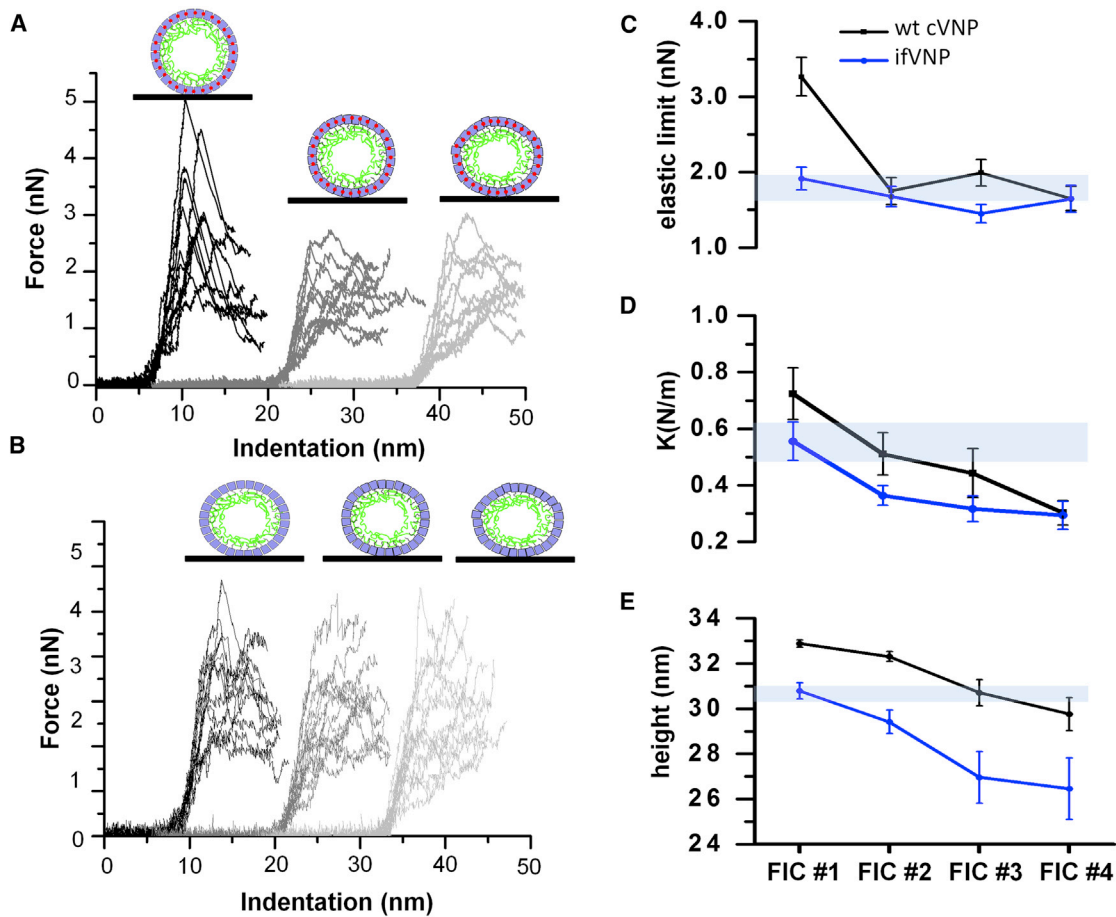
adsorption and the mechanical characterization addressed by nanoindentation experiments.

The high heterogeneity of charge density and hydrophobic patches within a virus shell permits the anchorage of the particle to substrates through a combination of van der Waals, electrostatic, and hydrophobic forces (39). Therefore, AFM imaging of adsorbed particles provides valuable parameters that reveal subtle details about VNP stability. This information is only valid for the sake of comparison between particles of the same virus, not between different viruses. Our experiments demonstrate that wild-type cVNPs and rVNPs show a height (~34 nm) in agreement with the expected diameter from x-ray data (31) and prove the structural reversibility of the swelling process. Contrariwise, the average height of ifVNPs (~29 nm) indicates that these structures decreased ~15% compared to their nominal size. Thus, the occurrence of structural rearrangements in the absence of calcium ions decreases the stability of TBSV capsid upon adsorption on the substrate. Moreover, the topographical AFM images showed collapsed sVNPs characterized by heights around 10 nm (Figs. 2 B and S2 C). Likewise, TEM images were correlated with AFM analysis and revealed that sVNPs were the less stable forms, as the staining agent penetrated inside the particles and some particles were dismantled. These data suggest that the swollen virus is the feeblest form of TBSV-NP.

The mechanics of each kind of VNP supported the aforementioned topological results. Indeed, if we assume the spring constant as a measurement of virus deformability,

Fig. 4 D indicates that ifVNPs were weaker than cVNPs by ~0.2 N/m. This lower rigidity might explain why ifVNPs presented a lower and more scattered height, which could be a consequence of structural rearrangements occurring after depletion of calcium ions.

Previous mechanical studies of VNPs have shown that the AFM tip usually removes individual structural components (16,19,26,36) after the elastic limit. In contrast, our data show that FICs induce an irreversible deformation of the structure without showing capsomeric vacancies. Since AFM imaging is able to resolve not only individual capsomers (26,33) but single proteins within the viral shell (26), the mechanical variation of TBSV-NPs after indentations must be related to subtle structural alterations consisting of intercapsomeric cracks too small to be resolved by the AFM. Although this phenomenon has been suggested for other viruses (40,41), our high-resolution AFM images present, to our knowledge, the first experimental evidence of the absence of capsomeric vacancies after breakage. We hypothesize that the resistance of individual capsomers to removal likely originates from the presence of inner capsid proteins interacting with ssRNA. These domains would keep the viral subunits joined to the viral core. In fact, when the virus shell was totally dismantled at the end of the loading cycle and the AFM tip could probably access the viral cargo, FICs revealed a monotonic nonlinear regime typical of deformation of solids (29). These final structures present a height that is compatible with the presence of RNA inside the viral particle.



Web 3C

**FIGURE 4** Comparison between the mechanical properties of wild-type cVNPs and ifVNPs. (A) The graph shows the overlap of the first three FICs (black, dark gray, and light gray, respectively) performed on 11 different wild-type cVNPs. Curves are laterally shifted for clarity. (B) Graphs show the first three FICs performed on 15 ifVNPs. Insets represent the progressive deformation of the particles along the loading process. The deformation is caused by the rearrangements of intercapsomeric interactions but does not entail the release of individual protein subunits. (C) Comparison of the evolution of the elastic limit between wt cVNPs (black line) and ifVNPs (blue line). (D) Comparison of the evolution of the elastic constant, obtained by fitting the linear part that precedes the plastic transition, for wt cVNPs (black line) and ifVNPs (blue line). (E) Comparison of the evolution of the height between wild-type cVNPs (black line) and ifVNPs (blue line), indicating the average height of the particles before performing the corresponding FICs. To see this figure in color, go online.

Our AFM results also show that the decrease in spring constant and elastic limit obtained after the chelation of calcium ions can be mimicked by deforming the virus with the AFM tip beyond its elastic limit (Fig. 4, C and D). This observation does not imply in turn that the structural changes induced by indentation are the same as those induced by ion sequestration, but suggests that both effects have similar mechanical consequences. Our hypothesis considers that the first indentation weakens some of the intercapsomeric interactions mediated by calcium ions, which consequently would reduce the resilience and rigidity of the particles. Subsequent deformations would then be probing a softer and more malleable structure that is held together, despite the alteration of these intercapsomeric bonds, due to the complex amalgam of coat proteins and inner tail proteins with the RNA genome. Therefore, calcium ions would act as elastic staples in-

serted between the capsomeric proteins, and their sequestration in ifVNPs would reduce the strength of the particle (42), leaving the main mechanical clamp for maintaining viral subunits together in the inner CP RNA binding domain. Finally, the capacity of TBSV to deform without losing capsomers indicates that the structural strategy of this virus is convenient for designing nanocontainers where the cargo stays isolated under aggressive physical assaults.

From a biophysical point of view, viral structures have to be labile enough to provide convenient metastability for the virus particle to accomplish its viral cycle. Some viruses, belonging to families other than TBSV, do not need virion swelling for cotranslational disassembly (43). TBSV and many other plant viruses, however, require swelling-induced structural changes to make RNA accessible to the cellular machinery (7,44,45). Our results for TBSV reflect this

situation by showing that the swollen forms of the virus, where the internal genome is still packed but reachable by the cellular proteins, are mechanically less stable than the compact forms.

## CONCLUSIONS

In this article, we report, to our knowledge, the first experimental evidence of the mechanical role of calcium ions bound to intracapsid sites. The sequestration of these ions reduces capsid resilience and rigidity. We found that an analogous decrease could also be induced by the first indentation on wild-type TBSV-NP, producing a permanent deformation of the particle without removing capsomers. In addition, our mechanical data are consistent with the metastability required for TBSV to accomplish its infection cycle. Calcium ions appear to be molecular determinants for virus strength, and their removal causes a mechanical instability that reduces virus resilience, which we hypothesize is governed by intercapsomeric interactions. In summary, our results point out the crucial structural role of calcium ions in viral shell stability. Also, the ability of TBSV to deform without losing capsomers would circumvent the release of cargo under hostile environments, thus identifying TBSV-NPs as suitable protein cages for cargo transportation at the nanoscale.

## SUPPORTING MATERIAL

Three figures and one table are available at [http://www.biophysj.org/biophysj/supplemental/S0006-3495\(15\)00584-6](http://www.biophysj.org/biophysj/supplemental/S0006-3495(15)00584-6).

## AUTHOR CONTRIBUTIONS

A.L. and E.C. performed the research. J.R.C. performed the TEM analysis. F.L., A.B., and L.S. contributed analytical tools. L.S., S.C., and P.J.deP. designed the research. A.L. and P.J.deP. wrote the article.

## ACKNOWLEDGMENTS

The authors thank the Ministerio de Economía y Competitividad of Spain for financial support of this research through project FIS2011-29493, the Spanish Interdisciplinary Network of the Biophysics of Viruses (Biofivinet FIS-2011-16090-E), and FIS2014-59562-R to P.J.P. and BFU 2011-25902 to J.R.C.. E.C. acknowledges a Short-Term Scientific Mission (STSM) supported by the European Cooperation in Science and Technology, Action TD 1002 AFM4NanoMed&Bio.

## REFERENCES

1. Flint, S. J., L. W. Enquist, ..., A. M. Skalka. 2004. Principles of Virology. ASM Press, Washington, D.C.
2. Douglas, T., and M. Young. 1998. Host-guest encapsulation of materials by assembled virus protein cages. *Nature*. 393:152–155.
3. Young, M., D. Willits, ..., T. Douglas. 2008. Plant viruses as biotemplates for materials and their use in nanotechnology. *Annu. Rev. Phytopathol.* 46:361–384.

4. Grasso, S., C. Lico, ..., L. Santi. 2013. A plant derived multifunctional tool for nanobiotechnology based on Tomato bushy stunt virus. *Transgenic Res.* 22:519–535.
5. Lüders, A., C. Müller, ..., Ch. Ziegler. 2012. Tomato bushy stunt viruses (TBSV) in nanotechnology investigated by scanning force and scanning electron microscopy. *Colloids Surf. B Biointerfaces.* 91:154–161.
6. Olson, A. J., G. Bricogne, and S. C. Harrison. 1983. Structure of tomato bushy stunt virus IV. The virus particle at 2.9 Å resolution. *J. Mol. Biol.* 171:61–93.
7. Robinson, I. K., and S. C. Harrison. 1982. Structure of the expanded state of tomato bushy stunt virus. *Nature*. 297:563–568.
8. Krüse, J., K. M. Krüse, ..., A. Tardieu. 1982. Divalent ion-dependent reversible swelling of tomato bushy stunt virus and organization of the expanded virion. *J. Mol. Biol.* 162:393–414.
9. Ivanovska, I. L., P. J. de Pablo, ..., G. J. L. Wuite. 2004. Bacteriophage capsids: tough nanoshells with complex elastic properties. *Proc. Natl. Acad. Sci. USA.* 101:7600–7605.
10. Carrasco, C., A. Carreira, ..., P. J. de Pablo. 2006. DNA-mediated anisotropic mechanical reinforcement of a virus. *Proc. Natl. Acad. Sci. USA.* 103:13706–13711.
11. Hernando-Pérez, M., R. Miranda, ..., P. J. de Pablo. 2012. Direct measurement of phage  $\phi$ 29 stiffness provides evidence of internal pressure. *Small.* 8:2366–2370.
12. Carrasco, C., M. Castellanos, ..., M. G. Mateu. 2008. Manipulation of the mechanical properties of a virus by protein engineering. *Proc. Natl. Acad. Sci. USA.* 105:4150–4155.
13. Castellanos, M., R. Pérez, ..., M. G. Mateu. 2012. Mechanical elasticity as a physical signature of conformational dynamics in a virus particle. *Proc. Natl. Acad. Sci. USA.* 109:12028–12033.
14. Cuellar, J. L., F. Meinhoevel, ..., E. Donath. 2010. Size and mechanical stability of norovirus capsids depend on pH: a nanoindentation study. *J. Gen. Virol.* 91:2449–2456.
15. Rayaprolu, V., B. M. Manning, ..., B. Bothner. 2010. Virus particles as active nanomaterials that can rapidly change their viscoelastic properties in response to dilute solutions. *Soft Matter.* 6:5286–5288.
16. Snijder, J., C. Uetrecht, ..., W. H. Roos. 2013. Probing the biophysical interplay between a viral genome and its capsid. *Nat. Chem.* 5:502–509.
17. Carrasco, C., M. Douas, ..., P. J. de Pablo. 2009. The capillarity of nanometric water menisci confined inside closed-geometry viral cages. *Proc. Natl. Acad. Sci. USA.* 106:5475–5480.
18. Roos, W. H., R. Bruinsma, and G. J. L. Wuite. 2010. Physical virology. *Nat. Phys.* 6:733–743.
19. Ivanovska, I. L., R. Miranda, ..., C. F. Schmidt. 2011. Discrete fracture patterns of virus shells reveal mechanical building blocks. *Proc. Natl. Acad. Sci. USA.* 108:12611–12616.
20. Ortega-Esteban, A., I. Horcas, ..., J. Gómez-Herrero. 2012. Minimizing tip-sample forces in jumping mode atomic force microscopy in liquid. *Ultramicroscopy.* 114:56–61.
21. Sader, J. E., J. W. M. Chon, and P. Mulvaney. 1999. Calibration of rectangular atomic force microscope cantilevers. *Rev. Sci. Instrum.* 70:3967–3969.
22. M. G. Mateu, editor 2013. Structure and Physics of Viruses. Springer, London.
23. Klug, W. S., R. F. Bruinsma, ..., G. J. L. Wuite. 2006. Failure of viral shells. *Phys. Rev. Lett.* 97:228101.
24. Vliegthart, G. A., and G. Gompper. 2006. Mechanical deformation of spherical viruses with icosahedral symmetry. *Biophys. J.* 91:834–841.
25. Pérez-Berná, A. J., A. Ortega-Esteban, ..., C. San Martín. 2012. The role of capsid maturation on adenovirus priming for sequential uncoating. *J. Biol. Chem.* 287:31582–31595.
26. Hernando-Pérez, M., E. Pascual, ..., P. J. de Pablo. 2014. The interplay between mechanics and stability of viral cages. *Nanoscale.* 6:2702–2709.

27. Butt, H. J. 1991. Electrostatic interaction in atomic force microscopy. *Biophys. J.* 60:777–785.
28. Sotres, J., and A. M. Baró. 2010. AFM imaging and analysis of electrostatic double layer forces on single DNA molecules. *Biophys. J.* 98:1995–2004.
29. Sneddon, I. N. 1965. The relation between load and penetration in the axisymmetric boussinesq problem for a punch of arbitrary profile. *Int. J. Eng. Sci.* 3:47–57.
30. Horcas, I., R. Fernández, ..., A. M. Baro. 2007. WSXM: a software for scanning probe microscopy and a tool for nanotechnology. *Rev. Sci. Instrum.* 78:013705.
31. Hopper, P., S. C. Harrison, and R. T. Sauer. 1984. Structure of tomato bushy stunt virus. V. Coat protein sequence determination and its structural implications. *J. Mol. Biol.* 177:701–713.
32. Villarrubia, J. S. 1997. Algorithms for scanned probe microscope image simulation, surface reconstruction, and tip estimation. *J. Res. Natl. Inst. Stand. Technol.* 102:425–454.
33. Ortega-Esteban, A., A. J. Pérez-Berná, ..., P. J. de Pablo. 2013. Monitoring dynamics of human adenovirus disassembly induced by mechanical fatigue. *Sci. Rep.* 3:1434.
34. Hernando-Pérez, M., S. Lambert, ..., P. J. de Pablo. 2014. Cementing proteins provide extra mechanical stabilization to viral cages. *Nat. Commun.* 5:4520.
35. Ivanovska, I. L., R. Miranda, ..., C. F. Schmidt. 2011. Discrete fracture patterns of virus shells reveal mechanical building blocks. *Proc. Natl. Acad. Sci. USA.* 108:12611–12616.
36. Castellanos, M., R. Pérez, ..., M. G. Mateu. 2012. Mechanical disassembly of single virus particles reveals kinetic intermediates predicted by theory. *Biophys. J.* 102:2615–2624.
37. Llauro, A., P. Guerra, ..., P. J. de Pablo. 2014. Mechanical stability and reversible fracture of vault particles. *Biophys. J.* 106:687–695.
38. A-Hassan, E., W. F. Heinz, ..., J. H. Hoh. 1998. Relative microelastic mapping of living cells by atomic force microscopy. *Biophys. J.* 74:1564–1578.
39. Müller, D. J., M. Amrein, and A. Engel. 1997. Adsorption of biological molecules to a solid support for scanning probe microscopy. *J. Struct. Biol.* 119:172–188.
40. Arkhipov, A., W. H. Roos, ..., K. Schulten. 2009. Elucidating the mechanism behind irreversible deformation of viral capsids. *Biophys. J.* 97:2061–2069.
41. Baclayon, M., W. H. Roos, and G. J. L. Wuite. 2010. Sampling protein form and function with the atomic force microscope. *Mol. Cell. Proteomics.* 9:1678–1688.
42. Zink, M., and H. Grubmüller. 2009. Mechanical properties of the icosahedral shell of southern bean mosaic virus: a molecular dynamics study. *Biophys. J.* 96:1350–1363.
43. Albert, F. G., J. M. Fox, and M. J. Young. 1997. Virion swelling is not required for cotranslational disassembly of cowpea chlorotic mottle virus in vitro. *J. Virol.* 71:4296–4299.
44. Aramayo, R., C. Mérigoux, ..., N. Boisset. 2005. Divalent ion-dependent swelling of tomato bushy stunt virus: a multi-approach study. *Biochim. Biophys. Acta.* 1724:345–354.
45. Bakker, S. E., R. J. Ford, ..., P. G. Stockley. 2012. Isolation of an asymmetric RNA uncoating intermediate for a single-stranded RNA plant virus. *J. Mol. Biol.* 417:65–78.